



# Cutting Force Model of SiCp/Al Composites in Ultrasonic Elliptical Vibration Assisted Cutting with Negative Rake Angle

Limin Zhang<sup>1,2</sup> · Zhuoshi Wang<sup>1,2</sup> · Jiakang Zhou<sup>3</sup> · Mingming Lu<sup>1,2</sup> · Yongsheng Du<sup>1,2</sup> · Hong Gong<sup>1,2</sup>

Received: 30 May 2024 / Accepted: 27 August 2024  
© The Author(s), under exclusive licence to Springer Nature B.V. 2024

## Abstract

SiCp/Al composites are widely used in many important engineering applications due to their excellent material properties. High-volume fraction SiCp/Al composites are recognised as a typical difficult-to-machining material with significant brittleness, and negative rake angles are more suitable for cutting brittle materials. Ultrasonic elliptical vibration cutting (UEVC) has proven to be a specialised machining method that can improve the machinability of difficult-to-machining materials. Elucidating the influence of the negative rake angle on the dynamic properties of composites during UEVC is therefore particularly important. In this paper, the direction of the combined cutting force is considered separately for negative rake angle tools, as well as UEVC's unique transient cutting thickness, variable cutting angle, transient shear angle and characteristic of friction reversal, a UEVC cutting force model based on negative tool rake angle has been developed. And the deviation of the main cutting force between the experimental value and the theoretical value is less than 15% by systematic turning experiments, which verifies the accuracy of the model. Finally, the influence of different machining parameters on the cutting force is determined using the established model. The results show its effect on the cutting force is more significant when the cutting speed is less than 200 mm/s, other things being equal. In addition, the cutting force tends to decrease significantly as the depth of cut from 5  $\mu\text{m}$  to 20  $\mu\text{m}$  increases. However, the cutting force fluctuated less when the feed was increased. This work provides the benchmark for negative rake angle cutting of SiCp/Al.

**Keywords** SiCp/Al Composites · Ultrasonic Elliptical Vibration Cutting (UEVC) · Negative Rake Angle · Cutting Force Model

## Nomenclature

$f$	Ultrasonic vibration frequency
$v_c$	Cutting speed
$t$	Cutting time
$\nu_{SiC}$	Poisson's ratio of particles
$TOC_t$	Transient cutting thickness
$a_p$	Cutting thickness

Extended author information available on the last page of the article

$\gamma_t$	Actual cutting rake Angle
$\gamma$	Mark the rake corner of the tool
$v_s$	Instantaneous shear velocity
$R$	Radius of particle
$\varphi_s$	Shear Angle in static friction zone
$\nu_{tool}$	Poisson's ratio of the tool
$\beta$	Friction Angle
$F$	Resultant cutting force
$F_s$	Shear force
$w$	Crack propagation width
$F_f$	Friction between chip and rake face
$F_{ns}$	Positive pressure from chips
$F_{f-3sic}$	Three-body rolling friction
$\sigma_{tool}$	The yield strength of the tool
$E_{SiC}$	Elastic modulus of particles
$V_p$	Volume fraction of SiC particles
$q$	Percentage of particles
$\delta_{p0}$	Critical penetration depth
$F_N^*$	The normal force of a particle
$v_{ct}$	The instantaneous speed of chips relative to the tool
$v_t$	The instantaneous relative speed of the tool to the workpiece
$A_{sic}$	The contact area between the front tool face and a particle
$F_n$	Normal force of chips on the front cutter face
$N_p$	The number of particles in knife-chip contact
$U_T$	The desticking force of individual particles
$U_D$	The breaking force of individual particles
$\theta_p$	Contact Angle between tool and particle
$F_N$	Normal force generated by SiC particles
$A_x$	Cutting speed direction ultrasonic amplitude
$F_p$	Cutting force Component in the direction of cutting speed
$\mu$	Tri-body rolling knife-chip friction coefficient
$H_T$	The proportion of SiC particles desticking
$K_T$	Critical debonding stress
$A_s$	Shear plane area
$\tau_s$	Shear flow stress
$A$	Yield strength
$B$	Hardening modulus
$C$	Strain sensitivity coefficient
$m$	Thermal softening coefficient
$n$	Hardening factor
$T$	Shear plane temperature
$T_{room}$	Room temperature
$\varepsilon$	Equivalent stress
$\dot{\varepsilon}^*$	Dimensionless strain rate
$\dot{\varepsilon}_0$	Material reference strain rate
$\dot{\varepsilon}$	Strain rate
$f$	Feed quantity
$\varphi$	Shear Angle
$\kappa_r$	Principal deflection Angle

$\kappa_r^*$	Equivalent contact Angle
$r_\epsilon$	Radius of the tip
$F_{f-2sic}$	Two-body sliding friction
$E_{tool}$	The elastic modulus of the tool
$\sigma_R$	Tensile strength
$a$	Initial crack length at interface
$\chi$	Slip line Angle
$P_A/k$	Hydrostatic pressure
$\psi$	Top corner of the holdup area
$l$	Length of retention zone
$\varphi_{kc}$	Shear Angle in conventional dynamic friction zone
$T_{melt}$	The melting temperature of the material
$A_{al}$	Contact area between substrate and front cutter face
$\varphi_{kr}$	Inverse shear Angle of dynamic friction zone
$\tau_c$	Average shear stress of knife-chip contact
$\theta(t)$	The transient direction Angle of the tool
$F_{DT}$	The breaking force and desticking force are
$\delta$	Angle between combined force direction and cutting direction
$H_D$	The proportion of SiC particle fracture
$A_y$	Ultrasonic amplitude in the direction of cutting depth
$F_t$	The component of the cutting force perpendicular to the cutting speed

## 1 Introduction

Silicon carbide particle-reinforced aluminium matrix composites (SiCp/Al) are important engineering materials consisting of an aluminium metal matrix and a volume fraction of silicon carbide particles as reinforcing phase [1, 2]. Because of its high strength, low density, high temperature resistance, corrosion resistance, and plastic processability, aluminum matrix composites (AMCs) are widely employed in industries like aircraft, automotive parts, and precision optical equipment [3, 4]. However, the low synergistic deformation capacity between the soft metal matrix and the hard ceramic particle makes the material removal process of SiCp/Al extremely difficult. Optimizing the machining process requires the cutting force model, particularly for challenging-to-machine materials as SiCp/Al composites with medium to high volume fractions. Establishing cutting force models is difficult due to the low machining efficiency and accuracy caused by the unique material properties of the SiC particles and the aluminum matrix [5–7].

The cutting forces of SiCp/Al composites have been modeled and researched by academics in recent decades [8]. Pramanik et al. [9] established a machining model for AMCs based on the shear plane analysis, slip line field theory and Griffith theory and analysed that the cutting force consists of cutting, ploughing and particle breaking forces, however, the friction of SiC particles between the tool and the chips was not analysed. By applying the theory of oblique cutting, Dabade et al. [10] have created a model for predicting cutting forces in composites. They also investigated the friction workpiece-tool-chip interfaces, considering two-body sliding and three-body rolling friction induced by SiC particles. However, they did not account for the ploughing forces of the matrix. In order to anticipate cutting forces, Sikder et al. [11] improved the cutting force model by utilizing the Johnson–Cook (J-C) model. The model computes the tool-chip friction and ploughing force

while accounting for temperature, high strain rate, and high strain produced during machining. For metal matrix composites, Ghandehariun et al. [12] suggested a novel cutting force model. The model determines cutting force for various system components, while considering plastic deformation of the matrix, friction at different interfaces, debonding and fracture of the particles. Wang et al. [13] developed a cutting force model that considers the geometrical and mechanical properties of the tool and workpiece, including the effect of SiC reinforced particles. The model predicts the cutting force as three components:  $F_x$ ,  $F_y$ ,  $F_z$ . Based on the randomness of SiCp/Al composite particle properties and the dynamic fluctuation features of the heat source, Yin et al. [14] created a new cutting force model for metal-matrix composites. The model is a dynamic cutting force model for orthogonal cutting of SiCp/Al. The cutting force models of SiCp/Al composites through traditional cutting () have been extensively studied up to this point, offering a theoretical foundation for the models. As technology progresses, more appropriate machining techniques for SiCp/Al composite cutting have also been investigated.

In comparison to TC, ultrasonic elliptical vibration cutting (UEVC) can effectively reduce average cutting force, the high frequency vibration generated by the ultrasonic waves acts on the tool, decreasing the frictional resistance during the cutting process by generating tiny vibrations between the tool and the workpiece [15–18]. For TC, there exists a critical cutting speed that, when surpassed, results in a notable rise in the cutting force. However, the instantaneous speed may exceed this crucial limit due to the intermittent separation feature of UEVC, resulting in crystal slips and dislocations within the material. This process renders the material more susceptible to fracture or ductile fracture along grain boundaries, while concomitantly enhancing its machinability, thereby reducing the cutting forces [19, 20]. In recent years, there has been significant research and exploration into the cutting force model for UEVC cutting of SiCp/Al composites. Based on the three-phase friction theory, Li et al. [21] created a cutting force prediction model for UEVC cutting of SiCp/Al composites. The friction components were calculated at three different points: tool-matrix contact, tool-particle contact, and tool-chip contact. The cutting transient thickness and transient shear angle effects were taken into account in the work conducted by Lin et al. [22], which suggested an analytical force model for the cutting force components of inclined UEVC. The transient cutting force of inclined UEVC is somewhat more than that of orthogonal UEVC, but it is more advantageous for chip flow, according to the results.

The literature review shows that the effect of tool geometry (negative rake angle) has not been considered in previous cutting force models for UEVC cutting of SiCp/Al composites. In contrast, for SiCp/Al, the tool rake angle is particularly important for the selection of cutting parameters [23]. A tool with a positive rake angle exerts tensile stress on the uncut material, and the shearability of the material greatly reduces the frictional resistance between tool and chip by suppressing the sticky chip phenomenon [24]. Conversely, a negative rake tool exerts compressive stresses on the uncut material and inhibits crack formation and propagation, effectively promoting material removal by plastic flow rather than brittle fracture, and is therefore commonly used in the cutting process of hard and brittle materials [25].

It is noted that, at present, there is no literature report on the cutting force model for UEVC dynamic cutting of SiCp/Al with negative rake angle. This study develops a cutting-force model to aid in the optimisation of UEVC cutting of SiCp/Al composites with negative rake angle.

There are five sections in this study. After this introduction, Section 2 goes on UEVC's motion characteristics. In Section 3, the methodology employed for the cutting force model is outlined. In Section 4 outlines the experimental apparatus, validates the precision of the model

through one-factor experiments, and clarifies how cutting parameters affect the cutting force estimation. Section 5 has conclusions.

## 2 UEVC Motion Characteristics

### 2.1 Principle of Elliptical Vibration Cutting

UEVC utilises piezoelectric ceramics to apply excitation to amplitude transformer. As a result, there is a high frequency vibration of the tool along the depth of cut and speed directions. Each vibration cycle's motion trajectory can be made to resemble a circle or an ellipse by varying the phase cycle difference. The cutting speed is matched with the purpose of continuous material removal [26]. The X and Y directions are used to set the cutting speed and depth, respectively. In this paper, the amplitudes in the direction of feed rate and depth of cut are 3 and 1, respectively. The process of UEVC is depicted in Fig. 1.

The tool's trajectory in relation to the workpiece [27]:

$$\begin{cases} X(t) = A_x \cos(2\pi ft + \phi) - v_c t \\ Y(t) = A_y \cos(2\pi ft) \end{cases} \quad (1)$$

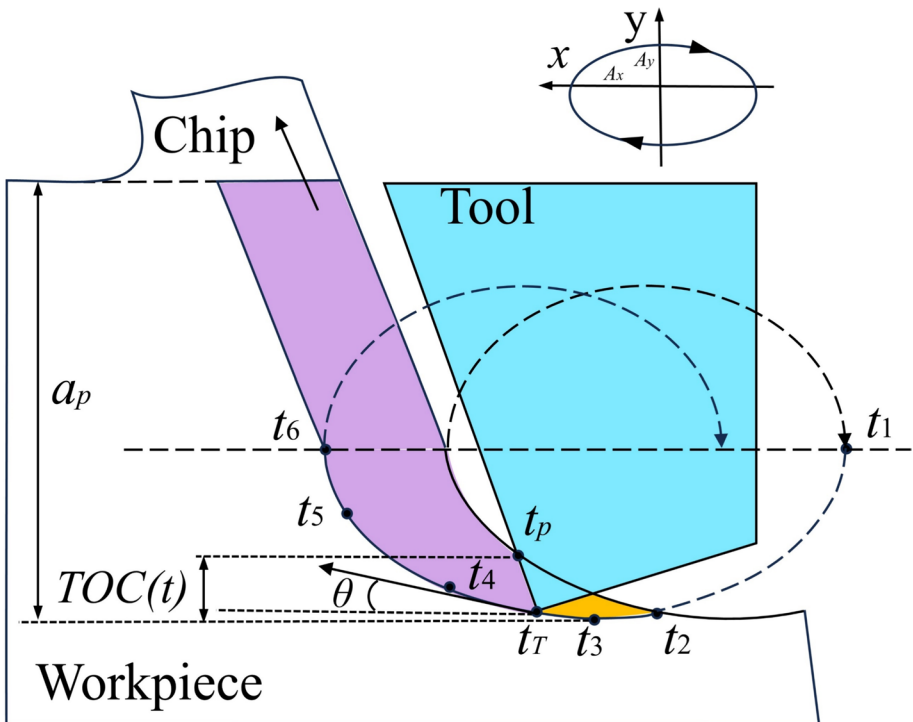


Fig. 1 Schematic diagram of UEVC process

where, the variables used in this study are  $A_x, A_y, f, v_c, t$ .  $A_x$  represents the direction of the cutting speed's ultrasonic amplitude, while  $A_y$  represents the ultrasonic amplitude in the direction of depth of cut. The variable  $f$  represents the ultrasonic vibration frequency,  $v_c$  represents the cutting speed,  $t$  represents the cutting time,  $\phi$  represents the phase difference.

Tool speed relative to workpiece is expressed as:

$$\begin{cases} v_x(t) = -2\pi f A_x \sin(2\pi ft) - v_c \\ v_y(t) = -2\pi f A_y \sin(2\pi ft) \end{cases} \quad (2)$$

The tool's transient direction angle is defined as the tangent direction of its trajectory:

$$\theta(t) = \tan^{-1} \left( \frac{v_y(t)}{v_x(t)} \right) \quad (3)$$

### 2.2 Transient Cutting Thickness and Variable Cutting Angle

During the UEVC process, the cutting thickness in each cycle undergoes constant change. As depicted in Fig. 1, the last cutting cycle ends at time  $t_1$ , followed by the beginning of the next cycle. At this point, the tool has not yet made contact with the workpiece. At time  $t_2$ , After the tool touches the workpiece, it begins cutting. At time  $t_3$ , when the tool's tip hits the cutting path's lowest point, resulting in the largest variable depth of cut. From  $t_4$  to  $t_5$ , the maximum thickness of the cut is reached and the transient cutting velocity is inverted with respect to the tool speed, resulting in knife-chip friction. At this point, the chip is removed. From  $t_5$  to  $t_6$ , the cutting cycle is completed and the knife-chip separation occurs until moving to the starting point of the next cycle. For a specific position  $t_T$  in the cutting process, the transient cutting thickness at this point is defined as the perpendicular distance between two points. And  $t_p$  indicates the position of the chip contact edge in the previous cutting cycle. Therefore, the transient cutting thickness is obtained as  $TOC_t$ .

$$TOC_t = \begin{cases} 0 & t < t_2; t > t_6 \\ Y(t_p) - Y(t_T) & t_2 \leq t \leq t_4 \\ a_p - [Y(t_T) - Y(t_3)] & t_4 \leq t \leq t_6 \end{cases} \quad (4)$$

The transient cutting thickness  $TOC_t$  of UEVC is less than the cutting thickness  $a_p$  of TC.

During the UEVC process, the cutting angle changes continuously with time [28], including the tool rake and tool clearance angles. This can be expressed in one cutting cycle as:

$$\gamma_t = \begin{cases} \gamma + \left| \arctan \frac{2\pi f A_y \cos 2\pi ft}{-2\pi f A_x \sin 2\pi ft + v_c} \right| & t_2 \leq t < t_3 \\ \gamma & t = t_3 \\ \gamma - \left| \arctan \frac{2\pi f A_y \cos 2\pi ft}{-2\pi f A_x \sin 2\pi ft + v_c} \right| & t_3 < t \leq t_6 \end{cases} \quad (5)$$

Equation (5) shows that in an UEVC cycle, where  $\gamma$  represents the actual cutting rake angle and  $\gamma_t$  is the tool marked rake angle, the tool rake angle is at its maximum when the tool just touches the workpiece. When the cut deepens to its greatest depth, the theoretical

rake angle and the actual rake angle become equal. When the tool leaves the workpiece, the tool rake angle is at its minimum.

### 2.3 Transient Shear Angle and Characteristic of Friction Reversal

During each cycle of UEVC, the shear angle undergoes instantaneous changes. To better understand the process of shear angle variation, the UEVC cycle is divided into cutting and separation phases. The cutting phase can be further divided into three zones based on the state of friction: regular dynamic friction zone, static friction zone, and counter-rotating friction zone. The kinetic friction zone begins at time  $t_2$ , when the shear angle is consistent with regular cutting using the same parameters. The static friction zone occurs when there is no relative motion in the tool-chip contact zone. The counter-rotational friction zone starts at time  $t_5$ , when the tool-chip friction stops and reverses, ending at the chip separation point.,  $t_6$  It is important to note that  $t_6$  does not refer to the moment when the tool has completed half a cycle, but rather to the moment when the tool's velocity relative to the workpiece is zero in the cutting direction.

The velocity relationship in the UEVC process can be stated as follows, according to the velocity analysis of the orthogonal cutting process:

$$v_s = v_t + v_{ct} \quad (6)$$

where,  $v_s$  represents the instantaneous shear speed,  $v_t$  represents the tool's and the workpiece's immediate relative speeds, and  $v_{ct}$  represents the instantaneous speed of the chip relative to the tool.

Figure 2 displays the velocity diagrams for the UEVC and TC processes, with the fixed shear directions of the shear velocity represented by the dashed lines OS and OS'. In the TC stage, shown in Fig. 2a, the magnitudes and directions of  $v_s$ ,  $v_t$ ,  $v_{ct}$  remain constant, while the shear angle  $\varphi$  is also constant. For the UEVC stage, as shown in Fig. 2b, the tool has just made contact with the workpiece and is now in the conventional dynamic friction zone. The instantaneous relative velocity angle between the tool and the workpiece is  $\theta$ , and the instantaneous shear angle is represented by the dotted line OS. Therefore, at this point,  $\varphi_{kc}$  is considered the shear angle. Upon entering the static friction zone, as depicted in Fig. 2c, the chip velocity ( $v_{ct}$ ) relative to the tool becomes zero. The instantaneous shear velocity ( $v_s$ ) is in the same direction as the instantaneous relative velocity ( $v_t$ ) between the tool and the workpiece. At this point, the shear angle ( $\varphi_s$ ) varies with the change of the instantaneous direction angle ( $\theta$ ). During the counter-rotating friction phase, as illustrated in Fig. 2d, the direction of the tool-chip friction is reversed, causing a reversal in the direction of the instantaneous velocity  $v_{ct}$  of the chip relative to the tool. At this point, the shear velocity is in the direction of the dashed line OS', and the shear angle is denoted as  $\varphi_{kr}$ .

The force diagram of the UEVC process based on the Merchant shear deformation theory is shown in Fig. 3 [7]. Figure 3a shows the conventional dynamic friction zone. The total cutting force is labelled as  $F$ , while  $F_n$  and  $F_f$  represent the normal force acting on the rake face and the friction between the chip and the rake face, respectively. Shear force in the shear plane and the positive pressure exerted by the chip are labelled as  $F_s$  and  $F_{ns}$ , respectively. The force in the direction of the cutting speed and the force perpendicular to the cutting speed of the cutting force are labelled as  $F_p$  and  $F_t$ , respectively. The tool rake angle is  $\gamma$ , the friction angle is  $\beta$ , and the shear angle is  $\varphi_{kc}$ . In the reverse friction zone, as shown in Fig. 3b, the shear force is  $\varphi_{kr}$ . According to the

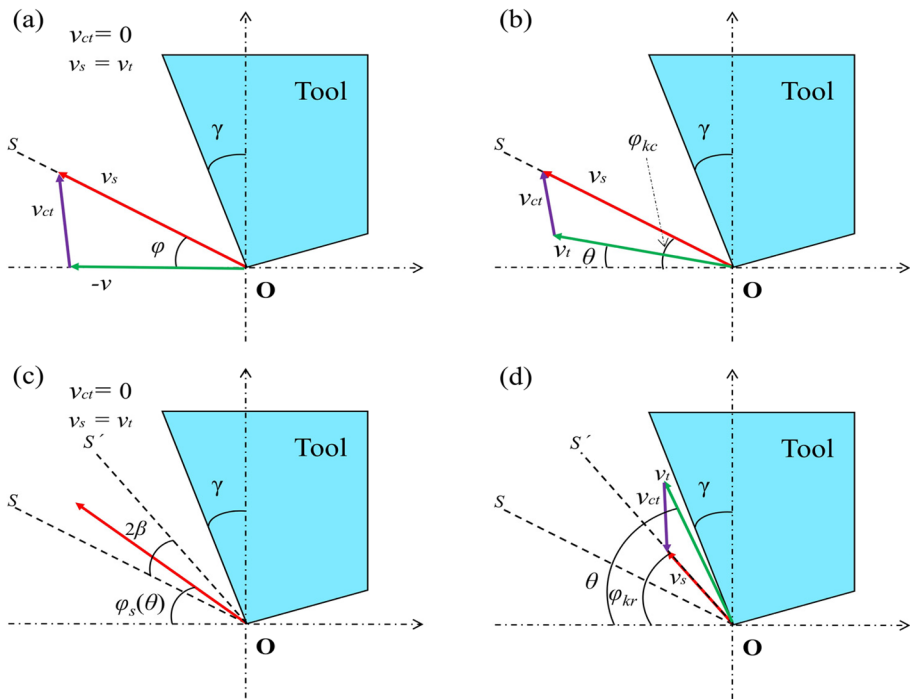


**Fig. 2** Velocity diagram of TC and UEVC processes: **a** TC process; **b** UEVC process regular kinetic friction zone; **c** UEVC process static friction zone; **d** UEVC process counter rotational friction zone

mechanics of materials, the angle between the direction of the combined force  $F$  and the shear force  $F_s$  is  $45^\circ$  [7]. It can be inferred from the geometric relationship in Fig. 3 that:

$$\begin{cases} \varphi_{kc} = \frac{\pi}{4} - \beta - \gamma \\ \varphi_{kr} = \frac{\pi}{4} + \beta - \gamma \end{cases} \quad (7)$$

The change in shear angle from the regular dynamic friction zone to the counter-rotating friction zone is:

$$\varphi_{kr} - \varphi_{kc} = 2\beta \quad (8)$$

In the UEVC force analysis study, Wei et al. [29] and Zhang et al. [30] both concluded that the shear angle changed, with Wei et al. reporting a change of  $\beta$  and Zhang et al. reporting a change of  $2\beta$ . These findings are consistent with the conclusions reached in this thesis. The difference in results can be attributed to the varying shear angle changes resulting from positive and negative rake angles, as well as the different directions of the combined forces due to the positive and negative angular rake angles.

The instantaneous shear angles in the three transition zones during the UEVC process are as follows, in combination with the above analysis:



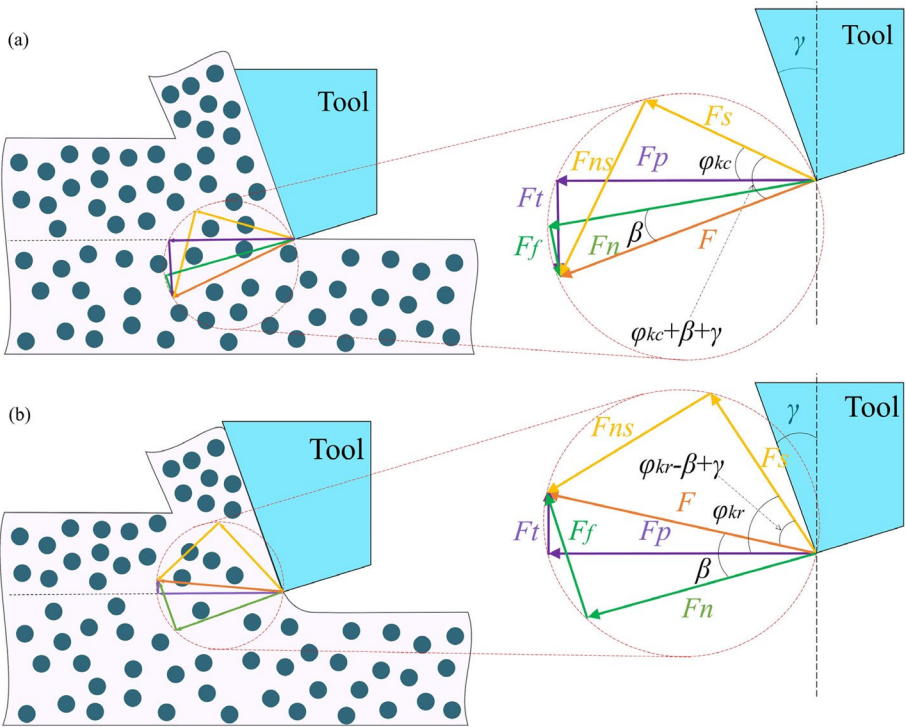


Fig. 3 Force diagram of the UEVC process: **a** Conventional friction zone; **b** Reverse friction zone

$$\varphi_t = \begin{cases} \varphi_{kc} & \theta_{(t_2)} \leq \theta_{(t)} \leq \varphi_{kc} \\ \theta_{(t)} & \varphi_{kc} \leq \theta_{(t)} \leq \varphi_{kr} \\ \varphi_{kr} & \varphi_{kr} \leq \theta_{(t)} \leq \theta_{(t_6)} \end{cases} \quad (9)$$

### 3 Cutting Force Model

The geometric relationship between cutting forces in SiCp/Al composites is examined in this section. SiC particle impact on the cutting forces and the time-varying characteristics of UEVC are considered. The cutting forces are divided into chip formation force, friction force, ploughing force and particle fracture force for separate analysis. To facilitate the analysis, the following assumptions are made: The tool’s rounded cutting edge radius is not considered. The SiCp/Al composite particles are assumed to be spherical with the same radius,  $R$ . In the second deformation zone, each SiC particle in the contact region between the rake face and the bottom of the chip shares the normal load equally. The cutting process does not take into account the effect of tool wear. The tool’s total cutting force,  $F$ , can be divided into three cutting component forces: the main cutting force,  $F_x$ , in the cutting speed direction; the draft resistance,  $F_y$ , in the depth of cut direction; and the feed resistance,  $F_z$ , in the feed direction.

### 3.1 Chip Formation Force

If the shear force  $F_s$  is uniformly distributed on the shear plane, the following can be obtained:

$$F_s = \tau_s A_s \quad (10)$$

where,  $A_s$  represents the shear plane area, and  $\tau_s$  represents the shear strength of the SiCp/Al composite. The shear flow stress can be calculated using the Johnson–Cook model:

$$\tau_s = \frac{1}{\sqrt{3}}(A + B\varepsilon^n)[1 + C \ln(\dot{\varepsilon}^*)][1 - (T^*)^m] \quad (11)$$

where,  $A$ ,  $B$ ,  $C$ ,  $m$ ,  $n$  represent the yield strength, hardening modulus, strain sensitivity factor, thermal softening coefficient and hardening factor of the material, the values of which are given in Table 1, and the homogenising temperature  $T^*$  can be expressed as:

$$T^* = \left( \frac{T - T_{room}}{T_{melt} - T_{room}} \right) \quad (12)$$

where,  $T$  represents the temperature of the shear plane,  $T_{room}$  represents the room temperature, and  $T_{melt}$  represents the melting temperature of the material.

where,  $\varepsilon$  represents the equivalent stress and  $\dot{\varepsilon}^*$  represents the dimensionless strain rate, which can be expressed as:

$$\begin{cases} \varepsilon = \frac{\cos \gamma}{\sin \varphi \cos(\varphi - \lambda)} \\ \dot{\varepsilon}^* = \frac{\dot{\varepsilon}}{\dot{\varepsilon}_0} \end{cases} \quad (13)$$

where,  $\dot{\varepsilon}_0$  is the reference strain rate of the material, typically taken to be  $1 \text{ s}^{-1}$ , and  $\dot{\varepsilon}$  is the strain rate, it can be calculated using the following formula:

$$\dot{\varepsilon} = \frac{2.59v_c \varepsilon \sin \varphi}{a_p} \quad (14)$$

$$A_s = f_{feed} \frac{a_p}{\sin \varphi} s \quad (15)$$

The parameters for the cutting process are defined as follows:  $a_p$  represents the cutting thickness,  $f_{feed}$  represents the cutting width (the feed during cutting), and  $\varphi$  represents the shear angle. In the UEVC process,  $a_p$  is replaced by  $TOC_t$ ,  $\varphi$  is replaced by  $\varphi_t$ , and  $\gamma$  is replaced by  $\gamma_t$ .

**Table 1** Rheological stress constants for the Al6061 Johnson–Cook model [31]

Material	A(MPa)	B(MPa)	C	m	n
Al6061	240	200	0.005	2	0.2

Figure 3 shows the conventional friction stage as Fig. 3a and the reverse friction stage as Fig. 3b. The angular relationship in the shear deformation process of the metal can be used to obtain 'F' and its two components.

$$F = \left\{ \begin{array}{l} \frac{\tau_s TOC_s f_{feed}}{\sin \varphi_t \cos(\varphi_t + \beta + \gamma_t)} \text{ (Conventional friction stage)} \\ \frac{\tau_s TOC_s f_{feed}}{\sin \varphi_t \cos(\varphi_t - \beta + \gamma_t)} \text{ (Reversed friction stage)} \end{array} \right\} \quad (16)$$

$$F_p^1 = \left\{ \begin{array}{l} \frac{\tau_s TOC_s f_{feed} \cos(\beta + \gamma_t)}{\sin \varphi_t \cos(\varphi_t + \beta + \gamma_t)} \text{ (Conventional friction stage)} \\ \frac{\tau_s TOC_s f_{feed} \cos(\beta - \gamma_t)}{\sin \varphi_t \cos(\varphi_t - \beta + \gamma_t)} \text{ (Reversed friction stage)} \end{array} \right\} \quad (17)$$

$$F_t^1 = \left\{ \begin{array}{l} \frac{\tau_s TOC_s f_{feed} \sin(\beta + \gamma_t)}{\sin \varphi_t \cos(\varphi_t + \beta + \gamma_t)} \text{ (Conventional friction stage)} \\ \frac{\tau_s TOC_s f_{feed} \sin(\beta - \gamma_t)}{\sin \varphi_t \cos(\varphi_t - \beta + \gamma_t)} \text{ (Reversed friction stage)} \end{array} \right\} \quad (18)$$

which in turn  $F_t^1$  can be decomposed into components in the Y and Z directions:  $F_{ty}^1, F_{tz}^1$ .

$$\begin{aligned} F_{ty}^1 &= F_t^1 \cos \kappa_r \\ F_{tz}^1 &= F_t^1 \sin \kappa_r \end{aligned} \quad (19)$$

where, the main deflection angle  $\kappa_r$  can be represented by the equivalent contact angle  $\kappa_r^*$  [32]. The straight cutting edge replaces the round and straight part of the cutting edge:

$$\kappa_r^* = \left\{ \begin{array}{l} \cot^{-1} \left[ \frac{r_\epsilon \operatorname{tg}(\kappa_r/2) + f_{feed}/2}{a_p} + \cot \kappa_r \right] a_p > r_\epsilon \\ \cot^{-1} \left[ \frac{2r_\epsilon a_p - a_p^2}{a_p} + f_{feed}/2 \right] a_p < r_\epsilon \end{array} \right\} \quad (20)$$

where,  $r_\epsilon$  is the radius of the tip circle.

### 3.2 Tool-chip Contact Friction

SiCp/Al composites are materials reinforced with SiC particles and an Al matrix. Therefore, friction in these composites can be divided into tool-particle friction and tool-matrix friction. The total friction force,  $F_f$ , is:

$$F_f = F_{f-sic} + F_{f-al} \quad (21)$$

### 3.2.1 Tool-particle Friction

The friction between the tool and the particles consists of two types: two-body sliding friction and three-body rolling friction. Figure 4 illustrates that two-body sliding friction occurs when particles adhere firmly to the bottom surface of the chip, creating a bulge with the rake face. On the other hand, three-body sliding friction occurs when particles generate a loose relative rolling friction force with the rake face. The friction between the tool and the particles is influenced by both types of friction:

$$F_{f-sic} = F_{f-2sic} + F_{f-3sic} \quad (22)$$

where,  $F_{f-2sic}$  represents two-body sliding friction and  $F_{f-3sic}$  represents three-body rolling friction.

#### 1) Two-body sliding friction force

Two-body sliding friction is similar to two-body abrasive wear and can be expressed as [33]:

$$F_{f-2sic} = N_p A_{sic} 3\sigma_{tool} q \quad (23)$$

where,  $\sigma_{tool}$  is the yield strength of the tool, and  $N_p$  is the number of particles in tool-chip contact, which can be expressed by the volume fraction  $V_p$  of SiC particles:

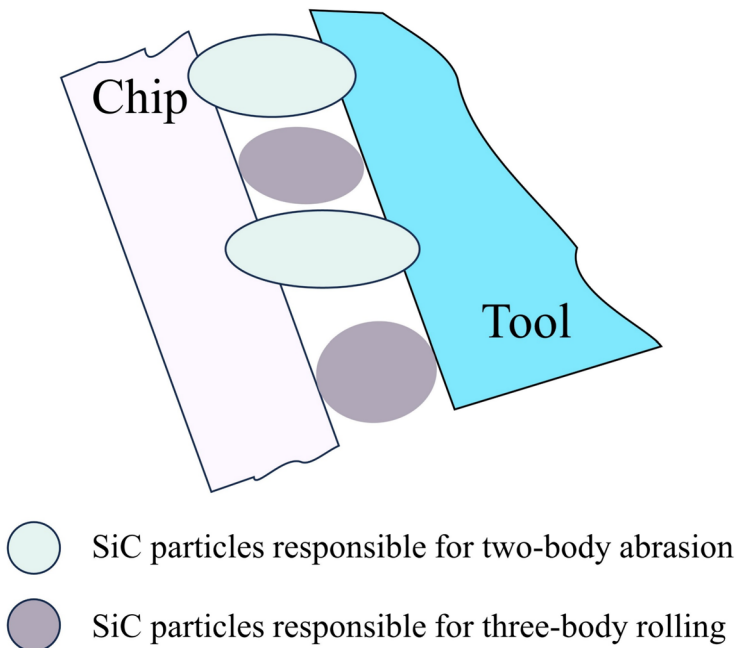


Fig. 4 Schematic diagram of tool-chip friction

$$N_p = \frac{V_p f_{feed} a_p}{\pi R^2} \tag{24}$$

The percentage of particles that create friction with the substrate in the tool-chip friction zone is represented by  $q$ :

$$q = 0.185 \times (2R)^{0.2885} \tag{25}$$

According to Fig. 5,  $\delta_{p0}$  represents the critical depth of penetration of SiC particles when they undergo complete plastic deformation at the front cutter face. Additionally,  $\theta_p$  denotes the contact angle between the tool and the particles,  $R$  represents the radius of the particles, and  $A_{sic}$  is the contact area between the front cutter face of the tool and a particle:

$$A_{sic} = \frac{R^2}{2} \left[ \frac{\pi}{180}(2\theta_p) - \sin(2\theta_p) \right] \tag{26}$$

$$\delta_{p0} = R \left( \frac{9\pi}{4} \right)^2 (\sigma_{tool})^2 \left[ \frac{E_{SiC}(1 - \nu_{tool})^2 + E_{tool}(1 - \nu_{SiC})^2}{E_{tool} + E_{SiC}} \right] \tag{27}$$

$$\theta_p = \arccos\left(1 - \frac{\delta_{p0}}{R}\right) \tag{28}$$

where,  $E_{tool}$  is the modulus of elasticity of the tool,  $E_{SiC}$  is the modulus of elasticity of the particles,  $\nu_{tool}$  is the Poisson's ratio of the tool and  $\nu_{SiC}$  is the Poisson's ratio of the particles.

2) The three-body rolling friction force

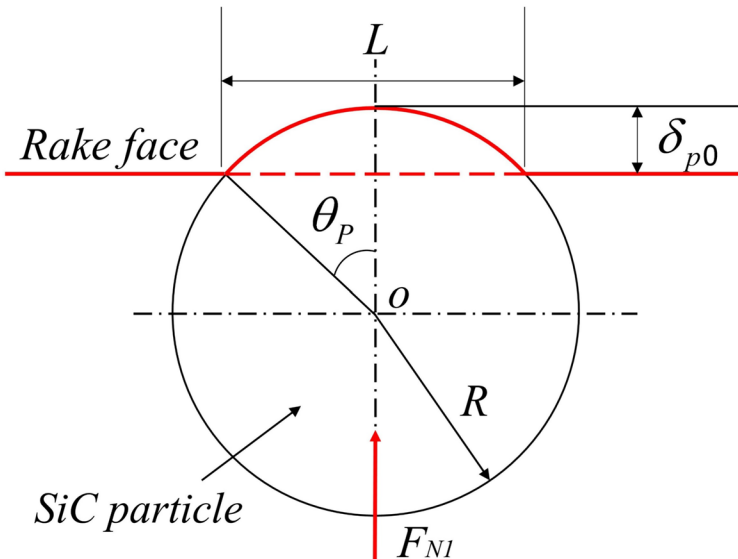


Fig. 5 Diagram of two-body sliding contact parameters

When cutting SiCp/Al, the SiC particles apply a normal force on the front face of the tool:

$$F_N = F_N^* N_p q \quad (29)$$

where,  $F_N^*$  is the normal force acting on one particle:

$$F_N^* = 2.9\pi R \sigma_{tool} \delta_{p0} \quad (30)$$

The friction coefficient for the three-body rolling tool-chip interaction can be calculated using the following equation:

$$\mu = \frac{2}{3\pi} \left(\frac{R}{L}\right)^2 \left\{ 1 - \left[ 1 - \left(\frac{R}{L}\right)^2 \right]^{1/2} \right\} \quad (31)$$

This can be obtained from the geometrical relations in Fig. 5:

$$L = \sqrt{R^2 - (R - \delta_{p0})^2} \quad (32)$$

Get the three-body rolling friction:

$$F_{f-3sic} = \mu F_N \quad (33)$$

### 3.2.2 Tool-matrix Friction Tool-material Plough Deformation Force

When cutting SiCp/Al composites, the friction between the tool's front face and the substrate is comparable to the friction experienced when cutting homogeneous materials [34]. This can be expressed using the following equation:

$$F_{f-al} = \tau_c A_{al} \quad (34)$$

where, the average shear stress of the knife-chip contact is represented by  $\tau_c$  and is calculated as  $\tau_c = 0.28\sigma_R$ , where  $\sigma_R$  is the tensile strength of the material. To determine the contact area  $A_{al}$  between the substrate and the rake face, subtract the contact area of the particles with the rake face from the total contact area:

$$A_{al} = A - A_{SiC} \quad (35)$$

Obtain this from Fig. 5:

$$A_{SiC} = \frac{\pi}{4} N_p L^2 q \quad (36)$$

The total friction during cutting SiCp/Al composites is divided into two directions: along the cutting speed and perpendicular to it, as determined by the above analysis:

$$\begin{cases} F_p^2 = F_f \sin \gamma \\ F_t^2 = F_f \cos \gamma \end{cases} \quad (37)$$

$F_t^2$  can be divided into components in the Y and Z directions:

$$\begin{cases} F_{ty}^2 = F_t^2 \cos \kappa_r \\ F_{tz}^2 = F_t^2 \sin \kappa_r \end{cases} \quad (38)$$

### 3.3 Tool-workpiece Ploughing Deformation Force

When cutting SiCp/Al composites, the SiC particles develop corresponding fracture and debonding forces, while the Al matrix is subjected to ploughing by the tool.

#### 3.3.1 Substrate Ploughing Force

The ploughing force resulting from the homogeneous plastic material of the Al matrix can be calculated using the slip line field model. While the slip line field model developed by LEE et al. [35] is widely used for tools with positive angles, it may not be applicable in all cases. To address this, we have used the slip line field model established by Fang et al. [36] for negative forward angles. The tangential and radial directions are then calculated separately:

$$\begin{cases} F_r = \tau_s ToC_f(1 + 2\chi + \tan \psi) + \tau_s lf \\ F_c = \tau_s ToC_f[(1 + 2\chi) \tan \psi - 1] + \tau_s lf [1 + 2\chi + \pi - 2\psi] \end{cases} \quad (39)$$

where, the slip line angle ( $\chi$ ) is expressed by the hydrostatic pressure  $P_A/k$ , typically ranging from 1.0 to 6.0:

$$\chi = \frac{(P_A/k) - 1}{2} \quad (40)$$

where, the stagnation zone's top angle  $\psi$  is:

$$\psi = \frac{\pi}{4} + \beta - \gamma_t - \chi \quad (41)$$

where, the stagnation zone's length ( $l$ ) is:

$$l = \frac{\sin((\pi/4) + \beta) - \sin(\psi + \gamma_t)}{\cos \psi \cos \gamma_t} * ToC_t \quad (42)$$

The tool's ploughing force on the Al substrate was divided into two directions: one along the cutting speed and the other perpendicular to it:

$$\begin{cases} F_r^3 = F_r \sin(\frac{\pi}{4} + \frac{\varphi_t}{2}) - F_c \cos(\frac{\pi}{4} + \frac{\varphi_t}{2}) \\ F_c^3 = F_r \cos(\frac{\pi}{4} + \frac{\varphi_t}{2}) - F_c \sin(\frac{\pi}{4} + \frac{\varphi_t}{2}) \end{cases} \quad (43)$$

$F_c^3$  can be divided into components in the Y and Z directions:

$$\begin{cases} F_{cy}^3 = F_c^3 \cos \kappa_r \\ F_{cz}^3 = F_c^3 \sin \kappa_r \end{cases} \quad (44)$$

### 3.3.2 Particle Breaking Force and Debonding Force

The fracture energy of a single particle is used to compute the fracture force of SiC particles:

$$U_D = \int_1^{2R} \frac{\pi K_D^2 a w (1 - v_{SiC})^2}{2R} f a \quad (45)$$

In a similar way, the debonding force of individual particles is:

$$U_T = \int_1^{2\pi R} \frac{\pi K_T^2 a w (1 - v_{SiC})^2}{2R} f a \quad (46)$$

where,  $a$  represents the initial crack length of the interface, assumed to be 1  $\mu\text{m}$ ,  $2R$  represents complete fracture, and  $2\pi R$  represents complete debonding.  $w$  represents the crack extension width of the SiC particles, assumed to be  $R$ . The fracture toughness of SiC particles, denoted as  $K_D$ , is 3  $\text{MPa}/\text{m}^{1/2}$ . The critical debonding stress, denoted as  $K_T$ , is given by the following equation:

$$K_T = \frac{2W_A [(1 + v_{Al}) \ln(1/V_p)]^{1/2}}{\delta^{-1} \coth(ns)} \quad (47)$$

Pramanik et al. [37] found that SiC particles in SiCp/Al composites are positioned on, above, or below the cutting path. If the particles are bound to fracture or debond during cutting, there is a 1/3 probability of this occurring. Therefore, the number of tool-induced particle debonding and fracture,  $N$ , can be calculated as:

$$N_{DT} = \frac{1}{3} * \frac{V_p f a_p}{\pi R^2} \quad (48)$$

Therefore, the fracture and debonding forces generated by the tool squeezing the particles are:

$$F_{DT} = f a_p N_{DT} (H_D U_D + H_T U_T) \quad (49)$$

The proportion of fractured SiC particles ( $H_D$ ) and debonded SiC particles ( $H_T$ ) should add up to one [38].

The SiC particles encounter very little force in the direction of the cut depth during the cutting process., but feel considerable force in the feed direction and cutting speed directions:

$$\begin{cases} F_{DT}^4 = F_{DT} \cos \delta \\ F_{DT_z}^4 = F_{DT} \sin \delta \end{cases} \quad (50)$$

where,  $S$  represents the angle between the direction of the combined force and the cutting direction:

$$\sin \delta = \frac{r_\epsilon (1 + \sin \gamma_t)}{2R + r_\epsilon} \quad (51)$$



## 4 Experiments and Discussions

### 4.1 Experimental Parameter Setting

Through cutting experiments, the cutting force model's dependability is confirmed in this part. The studies were carried out using a highly precise machine tool, as shown in Fig. 6a. A round bar of SiCp/Al composite with a 45% volume fraction (diameter of 12.7 mm and an average particle size of 15  $\mu\text{m}$ ) was clamped onto the machine tool for the experiments. The cutting tool is a PCD tool (CCGT09T304) with good wear resistance. The cutter had rake angles of  $-10^\circ$ ,  $-20^\circ$ ,  $-30^\circ$ , and  $-40^\circ$ , a clearance angle of  $7^\circ$ , and a tip arc radius of 0.4 mm. An ultrasonic vibration device was installed on a force gauge to achieve the UEVC, as depicted in Fig. 6b. The cutting force was measured using 3-axis dynamometer (Kistler 9109AA), as shown in Fig. 6c, for the purpose of data collection and measurement. To minimize the impact of machining parameters on force measurement, we conducted five cutting experiments using the same cutting parameters and calculated the average value. We used a one-factor experimental method, and Table 2 provides a list of the experimental parameters.



**Fig. 6** Experimental setup for cutting SiCp/Al composites by UEVC: **a** Ultra-precision machine tool; **b** UEVC schematic; **c** force measurement system

**Table 2** Experimental parameters of SiCp/Al composites

Parameters	Values
Feed rate (mm/r)	0.01
Cutting speed (mm/s)	200
Depth of cut ( $\mu\text{m}$ )	10
Rake angle ( $^\circ$ )	-10, -20, -30, -40
Amplitude x/y ( $\mu\text{m}$ )	3/1
Volume fraction of particles (%)	45
Frequency (kHz)	33.417

## 4.2 Model Validation

This paper validates the accuracy of the model by verifying the main cutting force, which accounts for the largest percentage of the total cutting force. Figures 7, 8, 9, and 10 depict the main cutting force plots of five cutting force experiments with tool rake angles of  $-10^\circ$ ,  $-20^\circ$ ,  $-30^\circ$ , and  $-40^\circ$ , respectively, along with the average and predicted values. Figures 7, 8, 9, and 10 show that the cutting force fluctuates significantly in experiments with the same tool rake angle. The reasons for this phenomenon are investigated below: 1. The particle distribution is random, resulting in varying force sizes in each experiment. 2. External factors such as human operation and environmental effects also have an impact. 3. The tool may wear out during the experiment. According to Fig. 11, the primary cutting force rises as the negative rake angle increases. This is because the negative angle increases, causing the ploughing effect to also increase.

Table 3 presents the deviation of each set of experimental data from the predicted values. As shown in Table 3, the difference between the main cutting forces calculated from the cutting force model and the experimentally measured main cutting forces is less than 15%. The maximum deviation of the main cutting force for a tool rake angle of  $-10^\circ$  is

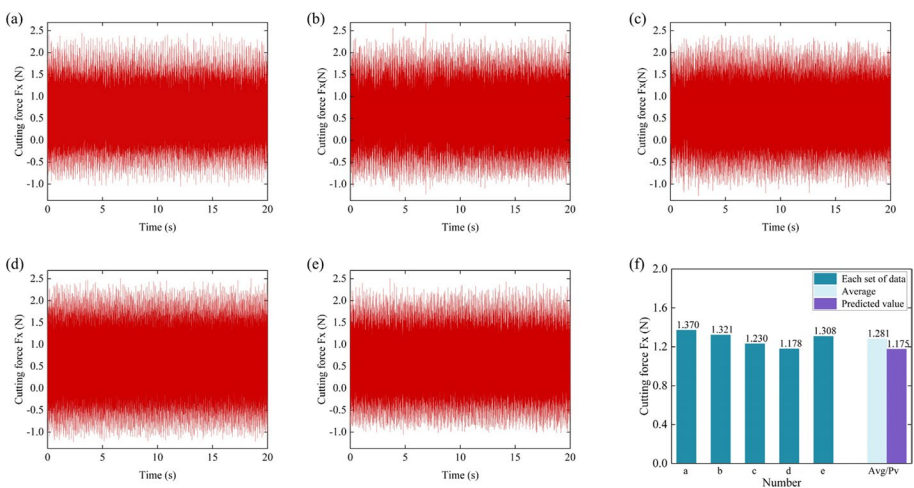


**Fig. 7** Cutting force diagrams for tool rake angle  $-10^\circ$  (a-e): cutting force diagrams for 5 experiments; f: average and predicted values

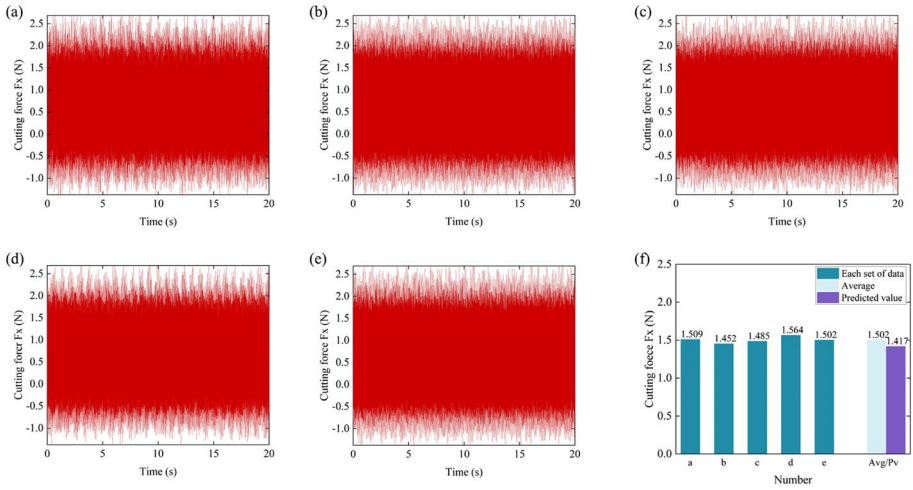


**Fig. 8** Cutting force diagrams for tool rake angle  $-20^\circ$  (a-e): cutting force diagrams for 5 experiments; f: average and predicted values

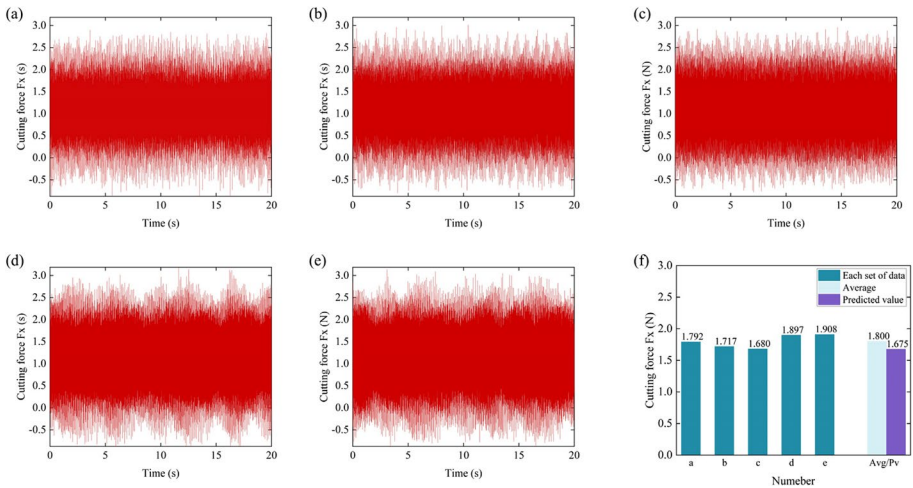


**Fig. 9** Cutting force diagrams for tool rake angle  $-30^\circ$  (a-e): cutting force diagrams for 5 experiments; f: average and predicted values

14.23% and the minimum is 0.2%, indicating that the cutting force model’s prediction is within an acceptable range.

Figure 11 shows the cutting force comparison between TC and UEVC for the parameters in Table 2. It can be seen that UEVC can effectively reduce the cutting force compared to TC. This is due to the intermittent cutting characteristic of the tool under UEVC which reduces the cutting force per unit time and the ultrasonic softening effect which reduces the cutting force when the tool cuts particles. According to Eq. (16), Eq. (37) and Eq. (50), an increase in the negative angle of the tool leading edge leads to an increase in the chip formation force, friction force and particle breakage force. The main cutting force of UEVC

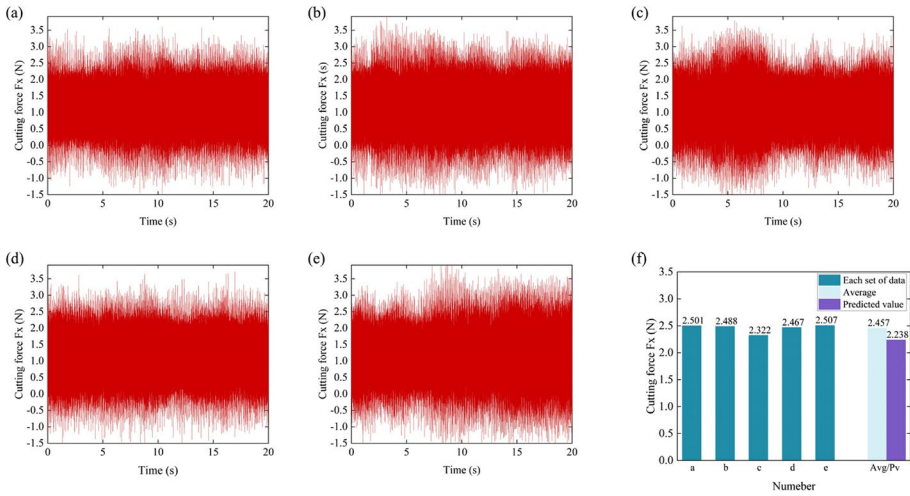


**Fig. 10** Cutting force diagrams for tool rake angle  $-40^\circ$  (a-e): cutting force diagrams for 5 experiments; f: average and predicted values

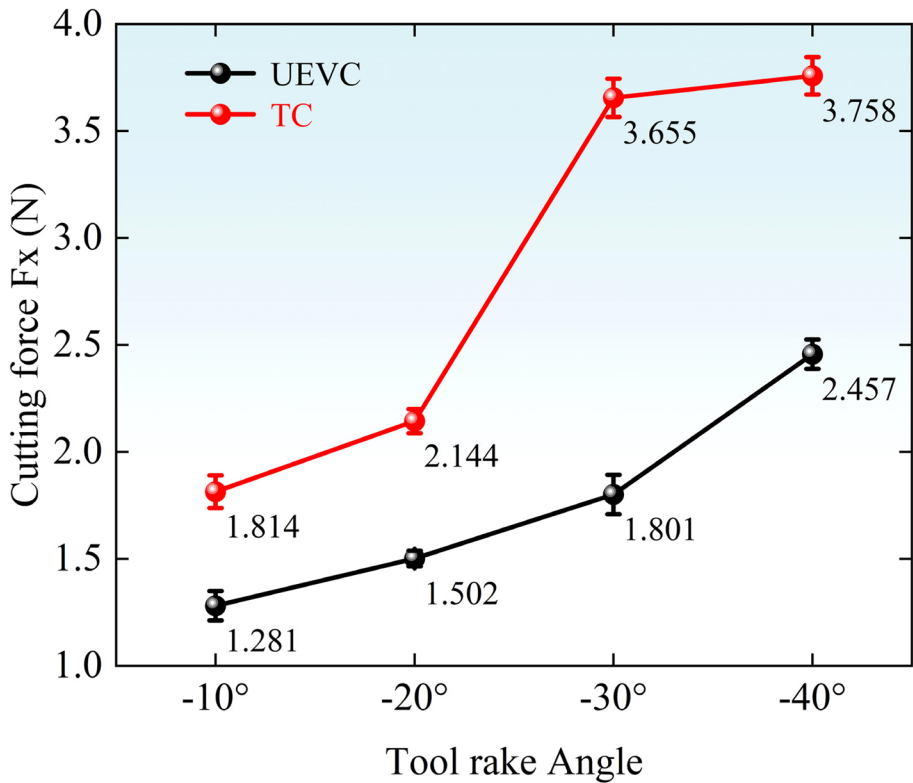


**Fig. 11** Comparison of the trend of average main cutting force of 4 groups of experiments with different tool rake angles for UEVC and TC

**Table 3** Comparison between the experimental and predicted values of the main cutting force

No	-10° Error (%)	-20° Error (%)	-30° Error (%)	-40° Error (%)
1	14.23	6.09	6.53	10.5
2	11.05	2.41	2.45	10.04
3	4.47	4.58	0.3	3.62
4	0.2	9.39	11.7	9.28
5	9.98	5.65	12.2	10.73
Avg	8.27	5.66	6.94	8.91

showed a moderate increase in the negative angle range of  $-10^\circ$  to  $-20^\circ$  and  $-20^\circ$  to  $-30^\circ$ , with an average increase of less than 0.3 N. However, when the negative angle was further increased to  $-30^\circ$  to  $-40^\circ$ , the main cutting force suddenly increased by nearly 0.6 N. The main cutting force of UEVC increased to  $-40^\circ$  with an increase in negative angle of  $-30^\circ$  to  $-40^\circ$ . Excessive negative angles can lead to a significant increase in cutting forces, which can have a negative impact on machining stability and tool life. Therefore, the size of the tool's rake angle must be balanced to ensure optimum cutting efficiency and machining quality.

### 4.3 Evaluating the Impact of Cutting Parameters on the Cutting Force Model

In order to assess how cutting parameters affect the cutting force, the cutting force model is computed in this part. The three factors taken into account are feed, depth of cut, and cutting speed. The cutting force is lowest when using the  $-10^\circ$  rake angle tool, as seen in Fig. 11. Therefore, the tool rake angle is chosen to be  $-10^\circ$ .

#### 4.3.1 Effect of Cutting Speed on Cutting Forces

This section examines the effect of cutting speed on cutting force. The cutting speed is varied at 100 mm/s, 200 mm/s, 300 mm/s, and 400 mm/s. The feed is set to 0.01 mm/r, the depth of cut is set to 10  $\mu\text{m}$ , and the cutting tool rake angle is  $-10^\circ$ . Figure 12 shows the variation curve of cutting force at different cutting speeds.

Figure 12 illustrates that when cutting speed goes from 100 mm/s to 200 mm/s, cutting force increases more than it does when cutting speed increases from 200 mm/s to 400 mm/s, which is similar to the conclusion reached by Zhou et al. [39]. Equation (16) and Eq. (39) can be used to evaluate this phenomenon: the chip formation force and substrate plowing force are directly impacted by the shear force, which rises with cutting speed. From a material perspective, SiCp/Al is a two-phase material. The Al matrix is softer and when subjected to stress during the cutting process, it flows plastically. However, it is hindered by the reinforcing-phase particles, resulting in the accumulation of dislocations and the formation of clusters. During this process, particles are subjected to stresses that can cause them to shear, fall off, or damage the substrate material. As cutting speed increases, dislocation accumulation becomes more severe, resulting in a corresponding increase in cutting force. However, at a certain cutting speed, the strain rate applied to the substrate becomes too large, resulting in the direct destruction of the substrate material. This weakens the particle enhancement, and as a result, the increase in cutting force is not

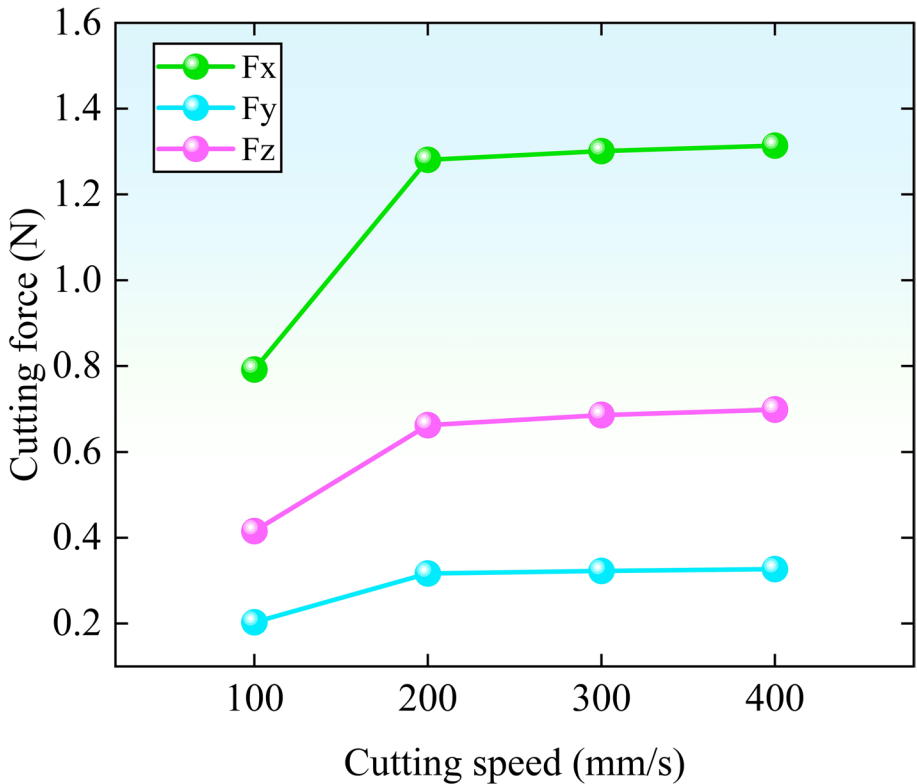


Fig. 12 Cutting force diagram at different cutting speeds

significant [40]. From an experimental perspective, increasing the cutting speed leads to a greater impact of the tool on the workpiece during the chip formation process in the UEVC. This results in a shorter intermittent time in the UEVC, which in turn increases the cutting force. However, at higher cutting speeds, the temperature in the cutting zone increases, causing the Al matrix in the SiCp/Al composites to soften. This results in a reduced impact of the tool on the workpiece, which in turn makes the increase in cutting force less pronounced. Simultaneously, due to the increased cutting speed, the SiCp/Al composite material produces shorter chip lengths, resulting in a quick separation from the workpiece [41]. This reduces the friction between the tool and the chip, leading to a decrease in cutting force. Consequently, a higher cutting speed can be considered in the parameter selection to enhance machining efficiency.

#### 4.3.2 Effect of Depth of Cut on Cutting Forces

This section examines the effect of varying depth of cut on cutting force. The values of 5 $\mu$ m, 10 $\mu$ m, 15 $\mu$ m and 20 $\mu$ m are tested while keeping the feed constant at 0.01 mm/r and

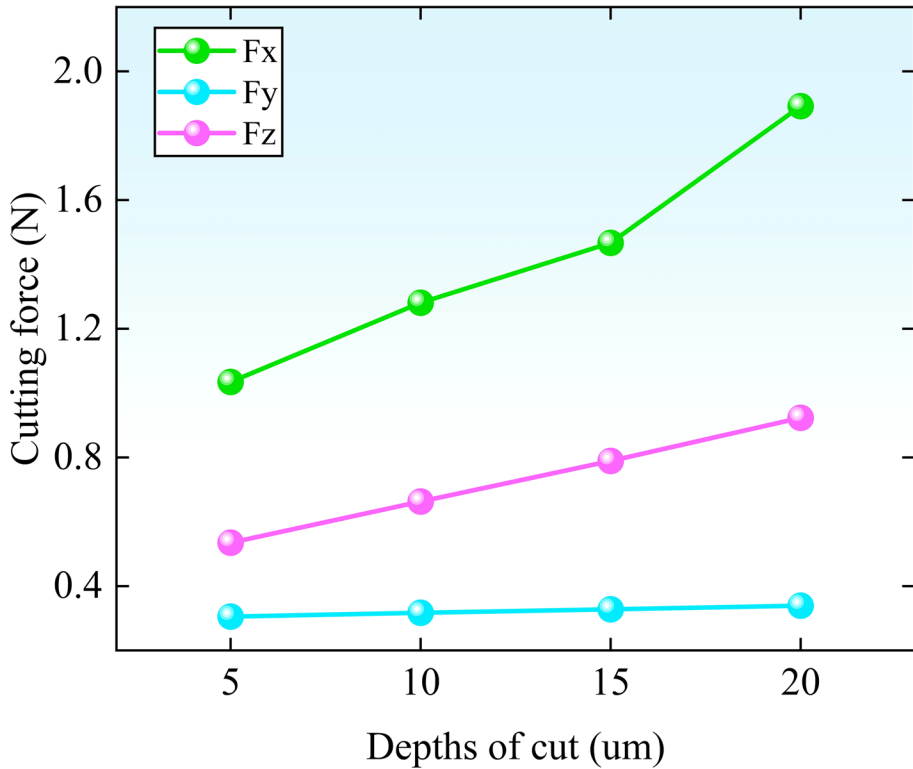


Fig. 13 Cutting force diagram at different depths of cut

the cutting speed at 200 mm/s. The cutting tool rake angle is set to  $-10^\circ$  and substituted into the cutting force model. The resulting change curve of cutting force is presented in Fig. 13.

Figure 13 exhibits how the cutting force rises as the depth of the cut. This increasing trend is similar to the findings of Liu et al. [42]. This can be explained by several factors. Firstly, the undeformed cutting thickness increases with the depth of cut, as shown in Eq. (4), resulting in a larger chip formation force. Furthermore, as per Eq. (24), when cutting SiCp/Al composites, more SiC particles come into touch with the knife when the depth of cut is increased, leading to increased friction. Additionally, a greater depth of cut leads to a higher metal removal rate and, consequently, an increase in cutting force. As the depth of cut increases, the range of contact between the tool and the workpiece also increases. This results in a gradual increase in cutting resistance that needs to be overcome. Additionally, the friction effect of chips on the front face also increases. Furthermore, as the depth of the cut increases, the force of interaction between the tool and the particles becomes more significant. The force between particles is also enhanced, and there is a certain level of connection strength between the matrix and the particles. As a result, a greater cutting force is required to form chips. To summarise, when the depth of cut gradually increases, the cutting force also increases dramatically. Thus, when choosing parameters, it's critical to take the depth of cut's impact on the cutting



force into account. It is recommended to adjust the depth of cut appropriately to manage the cutting force and enhance machining efficiency.

### 4.3.3 Effect of Feed on Cutting Forces

In this section, the feed rate is taken as the variable and its value is set to 0.005 mm/r, 0.01 mm/r, 0.015 mm/r, 0.02 mm/r. The depth of cut is set to 10 $\mu$ m, the cutting speed is set to 200 mm/s, and the tool rake angle is  $-10^\circ$ . The cutting force variation curve under various feeds is obtained by substituting these values into the cutting force model, as seen in Fig. 14.

Figure 14 shows that the effect of feed on cutting force is not significant. Although Eq. (16), Eq. (39) and Eq. (49) indicate that the feed amount affects the cutting force in several ways, the increments are small, resulting in little fluctuation in the cutting force. However, it is important to note that an excessively high feed rate can have a negative impact on the surface topography of the machined workpiece, which in turn affects the integrity of the machined surface. Therefore, it is necessary to choose a moderate feed rate during the machining process to balance the relationship between machining efficiency and quality. In summary, while the feed amount has a limited effect on the cutting force, it is still important to carefully select it during actual machining to ensure optimal machining results while minimizing fluctuations in the cutting force.

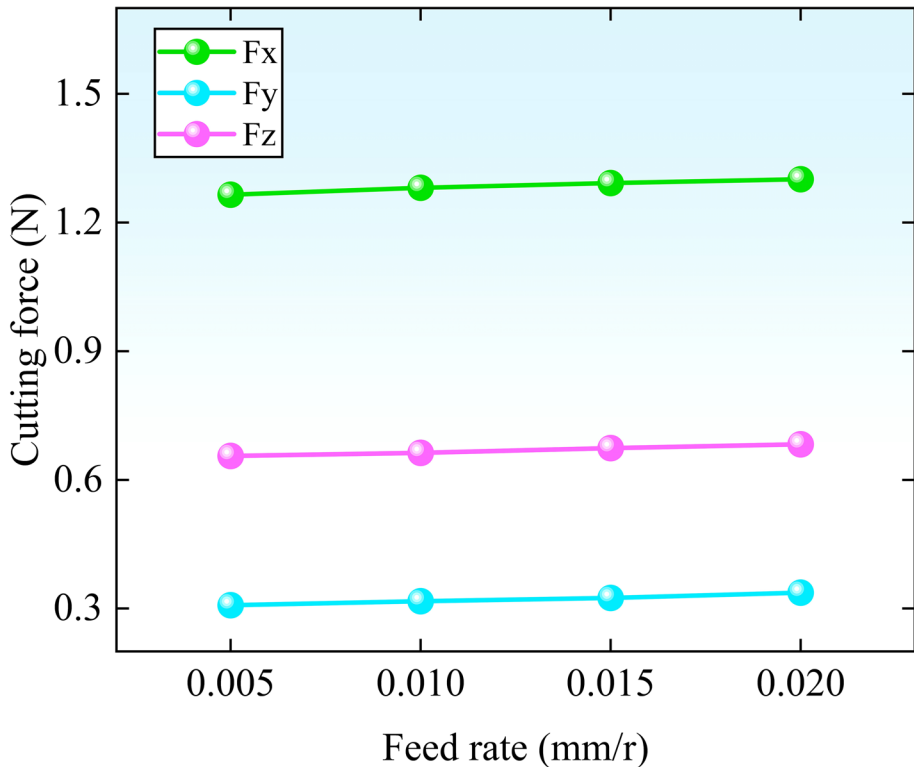


Fig. 14 Cutting force diagram at different feed



## 5 Conclusions

This paper presents a prediction model for cutting force during negative rake angle ultrasonic elliptical vibration-assisted cutting of SiCp/Al composites. The model is validated against experimental results. The following conclusions are drawn:

1. The model considers the interaction between the tool, matrix, and particles, as well as the instantaneous cutting thickness, variable cutting angle, and transient shear angle. Compared with the existing cutting force model, the slip line field model of negative rake angle is introduced, and combined with the principle of ultrasonic elliptic vibration, the cutting force model of negative rake angle UEVC cutting SiCp/Al composites is proposed.
2. The reliability of the model is confirmed by the relative deviation of the predicted main cutting force value, calculated based on the model, and the experimental value being less than 15%. The experimental results and cutting force model calculations indicate that the main cutting force increases with an increase in the negative rake angle. However, a negative rake angle that is too large is unsuitable for UEVC cutting of SiCp/Al composites.
3. The analysis examined the impact of cutting parameters (cutting speed, depth of cut, and feed) on cutting force. The findings indicate that cutting speed has a significant effect on cutting force when it is below 200 mm/s, but the effect is smaller when it exceeds 200 mm/s. Depth of cut has a significant impact on cutting force, while feed has a minor effect.

Overall, the cutting force model presented in this paper does not take into account the cutting edge radius of the tool, which may affect the accuracy of the prediction. Therefore, future research could focus on improving this point. Considering also that the vibration amplitude affects the shear angle and cutting force, future experiments and comparisons of vibration parameters with different frequencies and amplitudes will continue to be conducted to further optimise the model and improve the prediction accuracy. In addition, the effect of negative front face angle on chip, surface quality and tool wear should be thoroughly investigated in subsequent work.

**Acknowledgements** This work was supported by National Natural Science Foundation of China (Grant No. U21A20137), Key R&D projects of Jilin Provincial Department of Science and Technology(20240302037GX) , Jilin Provincial International Cooperation Key Laboratory for High-Performance Manufacturing and Testing (20220502003GH).

**Author Contributions** Limin Zhang and Zhuoshi Wang wrote the main manuscript text; Jiakang Zhou and Mingming Lu contributed to the preparation of experiment samples and data collection; Yongsheng Du contributed to the data curation; Hong Gong contributed to the supervision.

**Data Availability** No datasets were generated or analysed during the current study.

## Declarations

**Competing Interests** The authors declare no competing interests.

## References

- Dong, G., Zhang, H., Zhou, M., Zhang, Y.: Experimental investigation on ultrasonic vibration-assisted turning of SiCp/Al composites. *Mater. Manuf. Process.* **28**, 999–1002 (2013). <https://doi.org/10.1080/10426914.2012.709338>
- Du, Y., Lu, M., Lin, J., Yang, Y.: Experimental and simulation study of ultrasonic elliptical vibration cutting SiCp/Al composites: chip formation and surface integrity study. *J. Mater. Res. Technol.* **22**, 1595–1609 (2023). <https://doi.org/10.1016/j.jmrt.2022.12.008>
- Laghari, R.A., Li, J., Yongxiang, W.: Study of machining process of sicp/al particle reinforced metal matrix composite using finite element analysis and experimental verification. *Materials (Basel)* **13**, 1–39 (2020). <https://doi.org/10.3390/ma13235524>
- Wu, Q., Si, Y., Wang, G.S., Wang, L.: Machinability of a silicon carbide particle-reinforced metal matrix composite. *RSC Adv.* **6**, 21765–21775 (2016). <https://doi.org/10.1039/c6ra00340k>
- Liu, C., Gao, L., Jiang, X., Xu, W., Liu, S., Yang, T.: Analytical modeling of subsurface damage depth in machining of SiCp/Al composites. *Int. J. Mech. Sci.* **185**, 105874 (2020). <https://doi.org/10.1016/j.ijmecsci.2020.105874>
- Xu, W., Zhang, L.C., Wu, Y.: Elliptic vibration-assisted cutting of fibre-reinforced polymer composites: understanding the material removal mechanisms. *Compos. Sci. Technol.* **92**, 103–111 (2014). <https://doi.org/10.1016/j.compscitech.2013.12.011>
- Merchant, M.E.: Mechanics of the metal cutting process. I. Orthogonal cutting and a type 2 chip. *J. Appl. Phys.* **16**, 267–275 (1945). <https://doi.org/10.1063/1.1707586>
- Bains, P.S., Sidhu, S.S., Payal, H.S.: Fabrication and machining of metal matrix composites: a review. *Mater. Manuf. Process.* **31**, 553–573 (2016). <https://doi.org/10.1080/10426914.2015.1025976>
- Pramanik, A., Zhang, L.C., Arsecularatne, J.A.: Prediction of cutting forces in machining of metal matrix composites. *Int. J. Mach. Tools Manuf.* **46**, 1795–1803 (2006). <https://doi.org/10.1016/j.ijmactools.2005.11.012>
- Dabade, U.A., Dapkekar, D., Joshi, S.S.: Modeling of chip-tool interface friction to predict cutting forces in machining of Al/SiCp composites. *Int. J. Mach. Tools Manuf.* **49**, 690–700 (2009). <https://doi.org/10.1016/j.ijmactools.2009.03.003>
- Sikder, S., Kishawy, H.A.: Analytical model for force prediction when machining metal matrix composite. *Int. J. Mech. Sci.* **59**, 95–103 (2012). <https://doi.org/10.1016/j.ijmecsci.2012.03.010>
- Ghandeharian, A., Hussein, H.M., Kishawy, H.A.: Machining metal matrix composites: novel analytical force model. *Int. J. Adv. Manuf. Technol.* **83**, 233–241 (2016). <https://doi.org/10.1007/s00170-015-7554-8>
- Wang, J., Zuo, J., Shang, Z., Fan, X.: Modeling of cutting force prediction in machining high-volume SiCp/Al composites. *Appl. Math. Model.* **70**, 1–17 (2019). <https://doi.org/10.1016/j.apm.2019.01.015>
- Yin, W., Duan, C., Li, Y., Miao, K.: Dynamic cutting force model for cutting SiCp/Al composites considering particle characteristics stochastic models. *Ceram. Int.* **47**, 35234–35247 (2021). <https://doi.org/10.1016/j.ceramint.2021.09.066>
- Zhou, J., Lu, M., Lin, J., Wei, W.: On understanding the cutting mechanism of SiCp/Al composites during ultrasonic elliptical vibration-assisted machining. *J. Mater. Res. Technol.* **27**, 4116–4129 (2023). <https://doi.org/10.1016/j.jmrt.2023.10.277>
- Zhou, J., Lu, M., Lin, J., Wei, W.: Influence of tool vibration and cutting speeds on removal mechanism of SiCp/Al composites during ultrasonic elliptical vibration-assisted turning. *J. Manuf. Process.* **99**, 445–455 (2023). <https://doi.org/10.1016/j.jmapro.2023.05.084>
- Nath, C., Rahman, M.: Effect of machining parameters in ultrasonic vibration cutting. *Int. J. Mach. Tools Manuf.* **48**(9), 965–974 (2008). <https://doi.org/10.1016/j.ijmactools.2008.01.013>
- Chen, G., Ren, C., Zou, Y., et al.: Mechanism for material removal in ultrasonic vibration helical milling of Ti6Al4V alloy. *Int. J. Mach. Tools Manuf.* **138**, 1–13 (2019). <https://doi.org/10.1016/j.ijmactools.2018.11.001>
- Xia, C., Lin, J., Lu, M., Zhang, X., Chen, S.: Study on machinability of SiCp/Al composites by laser-induced oxidation-assisted turning. *J. Mater. Eng. Perform.* (2024). <https://doi.org/10.1007/s11665-024-09399-2>
- Zhou, J., Lu, M., Lin, J., Su, X., Wei, W.: Analytical modeling of cutting force in machining of SiCp/Al composites by ultrasonic elliptical vibration-assisted turning. *Proc. Inst. Mech. Eng. Part B J. Eng. Manuf.* (2023). <https://doi.org/10.1177/09544054231197337>
- Li, Y., Zhang, X., Wang, C.: Cutting force prediction model for elliptical vibration cutting sicp/al based on three-phase friction theory. *Appl. Sci.* **11**, 10737 (2021). <https://doi.org/10.3390/app112210737>

22. Jieqiong, L., Jinguo, H., Xiaoqin, Z., Zhaopeng, H., Mingming, L.: Study on predictive model of cutting force and geometry parameters for oblique elliptical vibration cutting. *Int. J. Mech. Sci.* **117**, 43–52 (2016). <https://doi.org/10.1016/j.ijmecsci.2016.08.004>
23. Lu, S., Li, Z., Zhang, J., Zhang, C., Li, G., Zhang, H., Sun, T.: Coupled effect of tool geometry and tool-particle position on diamond cutting of SiCp/Al. *J. Mater. Process. Technol.* **303**, 117510 (2022). <https://doi.org/10.1016/j.jmatprotec.2022.117510>
24. Sun, J., Ke, Q., Chen, W.: Material instability under localized severe plastic deformation during high speed turning of titanium alloy Ti-6.5AL-2Zr-1Mo-1V. *J. Mater. Process. Technol.* **264**, 119–128 (2019). <https://doi.org/10.1016/j.jmatprotec.2018.09.002>
25. Zhao, L., Hu, W., Zhang, Q., Zhang, J., Zhang, J., Sun, T.: Atomistic origin of brittle-to-ductile transition behavior of polycrystalline 3C–SiC in diamond cutting. *Ceram. Int.* **47**, 23895–23904 (2021). <https://doi.org/10.1016/j.ceramint.2021.05.098>
26. Shamoto, E., Suzuki, N., Hino, R.: Analysis of 3D elliptical vibration cutting with thin shear plane model. *CIRP Ann. - Manuf. Technol.* **57**, 57–60 (2008). <https://doi.org/10.1016/j.cirp.2008.03.073>
27. Huang, W., Yu, D., Zhang, X., et al.: Ductile-regime machining model for ultrasonic elliptical vibration cutting of brittle materials[J]. *J. Manuf. Process.* **36**, 68–76 (2018). <https://doi.org/10.1016/j.jmapro.2018.09.029>
28. Ma, C., Shamoto, E., Moriwaki, T., Wang, L.: Study of machining accuracy in ultrasonic elliptical vibration cutting. *Int. J. Mach. Tools Manuf.* **44**, 1305–1310 (2004). <https://doi.org/10.1016/j.jmachtools.2004.04.014>
29. Bai, W., Sun, R., Gao, Y., Leopold, J.: Analysis and modeling of force in orthogonal elliptical vibration cutting. *Int. J. Adv. Manuf. Technol.* **83**, 1025–1036 (2016). <https://doi.org/10.1007/s00170-015-7645-6>
30. Zhang, X., Senthil Kumar, A., Rahman, M., Nath, C., Liu, K.: An analytical force model for orthogonal elliptical vibration cutting technique. *Manuf. Process.* **14**, 378–387 (2012). <https://doi.org/10.1016/j.jmapro.2012.05.006>
31. Zhou, L., Cui, C., Zhang, P.F., Ma, Z.Y.: Finite element and experimental analysis of machinability during machining of high-volume fraction SiCp/Al composites. *Int. J. Adv. Manuf. Technol.* **91**, 1935–1944 (2017). <https://doi.org/10.1007/s00170-016-9933-1>
32. Colwell, L.V.: Predicting the angle of chip flow for single-point cutting tools. *J. Fluids Eng.* **76**, 199–203 (1954). <https://doi.org/10.1115/1.4014795>
33. Duan, C., Sun, W., Fu, C., Zhang, F.: Modeling and simulation of tool-chip interface friction in cutting Al/SiCp composites based on a three-phase friction model. *Int. J. Mech. Sci.* **142–143**, 384–396 (2018). <https://doi.org/10.1016/j.ijmecsci.2018.05.014>
34. Astakhov, V.P., Xiao, X.: A methodology for practical cutting force evaluation based on the energy spent in the cutting system. *Mach. Sci. Technol.* **12**, 325–347 (2008). <https://doi.org/10.1080/10910340802306017>
35. Lee, E.H., Shaffer, B.W.: The theory of plasticity applied to a problem of machining[J]. (1951). <https://doi.org/10.1115/1.4010357>
36. Fang, N.: Tool-chip friction in machining with a large negative rake angle tool. *Wear* **258**, 890–897 (2005). <https://doi.org/10.1016/j.wear.2004.09.047>
37. Pramanik, A., Zhang, L.C., Arsecularatne, J.A.: An FEM investigation into the behavior of metal matrix composites: Tool-particle interaction during orthogonal cutting. *Int. J. Mach. Tools Manuf.* **47**, 1497–1506 (2007). <https://doi.org/10.1016/j.ijmactools.2006.12.004>
38. Wee, S., Dowding, J.M., Nadakavukaren, M.J., Wilkinson, B.J.: Characterization of cell surface material removed by water and NaCl washing of *Paracoccus denitrificans* grown under conditions of divalent cation deficiency and sufficiency. *Antonie Van Leeuwenhoek* **65**, 35–39 (1994). <https://doi.org/10.1007/BF00878277>
39. Zhou, Y., Gu, Y., Lin, J., Zhao, H., Liu, S., Xu, Z., Yu, H., Fu, X.: Finite element analysis and experimental study on the cutting mechanism of SiCp/Al composites by ultrasonic vibration-assisted cutting. *Ceram. Int.* **48**, 35406–35421 (2022). <https://doi.org/10.1016/j.ceramint.2022.08.142>
40. Yuan, Z., Xiang, D., Peng, P., Zhang, Z., Li, B., Ma, M., Zhang, Z., Gao, G., Zhao, B.: A comprehensive review of advances in ultrasonic vibration machining on SiCp/Al composites. *J. Mater. Res. Technol.* **24**, 6665–6698 (2023). <https://doi.org/10.1016/j.jmrt.2023.04.245>
41. Kannan, S., Kishawy, H.A., Deiab, I.: Cutting forces and TEM analysis of the generated surface during machining metal matrix composites. *J. Mater. Process. Technol.* **209**, 2260–2269 (2009). <https://doi.org/10.1016/j.jmatprotec.2008.05.025>
42. Liu, C.S., Zhao, B., Gao, G.F., Jiao, F.: Research on the characteristics of the cutting force in the vibration cutting of a particle-reinforced metal matrix composites SiCp/Al. *J. Mater. Process. Technol.* **129**, 196–199 (2002). [https://doi.org/10.1016/S0924-0136\(02\)00649-0](https://doi.org/10.1016/S0924-0136(02)00649-0)

**Publisher's Note** Springer Nature remains neutral with regard to jurisdictional claims in published maps and institutional affiliations.

Springer Nature or its licensor (e.g. a society or other partner) holds exclusive rights to this article under a publishing agreement with the author(s) or other rightsholder(s); author self-archiving of the accepted manuscript version of this article is solely governed by the terms of such publishing agreement and applicable law.

## Authors and Affiliations

**Limin Zhang**<sup>1,2</sup> · **Zhuoshi Wang**<sup>1,2</sup> · **Jiakang Zhou**<sup>3</sup> · **Mingming Lu**<sup>1,2</sup> · **Yongsheng Du**<sup>1,2</sup> · **Hong Gong**<sup>1,2</sup>

✉ Jiakang Zhou  
zhoujiakang07@163.com

✉ Mingming Lu  
lumm@ccut.edu.cn

<sup>1</sup> Jilin Provincial Key Laboratory of Micro-Nano and Ultra-Precision Manufacturing, School of Mechatronic Engineering, Changchun University of Technology, Yan'an Ave 2055, Changchun, Jilin 130012, PR China

<sup>2</sup> Provincial Key Laboratory of International Science and Technology Cooperation for High Performance Manufacturing and Testing, School of Mechatronic Engineering, Changchun University of Technology, Yan'an Ave 2055, Changchun, Jilin 130012, PR China

<sup>3</sup> School of Machinery and Automation, Weifang University, Weifang 261061, China